

# Conical Intersection and Potential Energy Surface Features of a Model Retinal Chromophore: Comparison of EOM-CC and Multireference Methods

Samer Gozem,<sup>†</sup> Anna I. Krylov,<sup>\*,‡</sup> and Massimo Olivucci<sup>\*,†,§</sup>

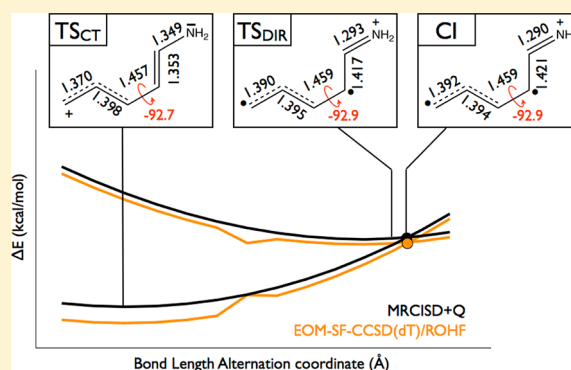
<sup>†</sup>Department of Chemistry, Bowling Green State University, Bowling Green, Ohio 43403, United States

<sup>‡</sup>Department of Chemistry, University of Southern California, Los Angeles, California 90089-0482, United States

<sup>§</sup>Dipartimento di Chimica, Università di Siena, via De Gasperi 2, I-53100 Siena, Italy

## Supporting Information

**ABSTRACT:** This work investigates the performance of equation-of-motion coupled-cluster (EOM-CC) methods for describing the changes in the potential energy surfaces of the penta-2,4-dieniminium cation, a reduced model of the retinal chromophore of visual pigments, due to dynamical electron correlation effects. The ground-state wave function of this model includes charge-transfer and diradical configurations whose weights vary along different displacements and are rapidly changing at the conical intersection between the ground and the first excited states, making the shape of the potential energy surface sensitive to a balanced description of nondynamical and dynamical correlation. Recently, variational (MRCISD) and perturbative (MRPT2) approaches for including dynamical correlation in CASSCF-based calculations were tested along three representative ground state paths. Here, we use the same three paths to compare the performance of single-reference EOM-CC methods against MRCISD and MRCISD+Q. We find that the spin-flip variant of EOM-CCSD with perturbative inclusion of triple excitations (dT or fT) produces potential energy profiles of the two lowest electronic states in quantitative agreement with MRCISD+Q (our highest-quality reference method). The nonparallelity errors and differences in vertical energy differences of the two surfaces along these scans are less than 1.4 kcal/mol (EOM-SF-CCSD(dT) versus MRCISD+Q). For comparison, the largest error of MRCISD versus MRCISD+Q is 1.7 kcal/mol. Our results show that the EOM-CC methods provide an alternative to multireference approaches and may be used to study photochemical systems like the one used in this work.



## INTRODUCTION

The penta-2,4-dieniminium cation (PSB3) is a protonated imine with three conjugated double bonds. It has been used extensively as a computational model of the retinal protonated Schiff base (rPSB) chromophore found in visual pigments.<sup>1–10</sup> (see Scheme 1A). The ground-state and first excited state potential energy surfaces of PSB3 have been recently investigated (focusing on the ground state) to find out how well multireference perturbation theory describes regions with variable charge-transfer/diradical character accompanied by rapidly changing dynamical electron correlation, in particular around conical intersections (CIs).<sup>10</sup> In the present work, the same energy surfaces are computed using equation-of-motion coupled-cluster (EOM-CC) methods to investigate the performance of these formally single-reference approaches for such problematic features arising due to interactions between nearly degenerate states of different character.

Gas-phase quantum mechanical (QM) studies on PSB3 as well as hybrid quantum mechanics/molecular mechanics (QM/MM) studies on the rPSB chromophore in bovine rhodopsin<sup>11</sup>

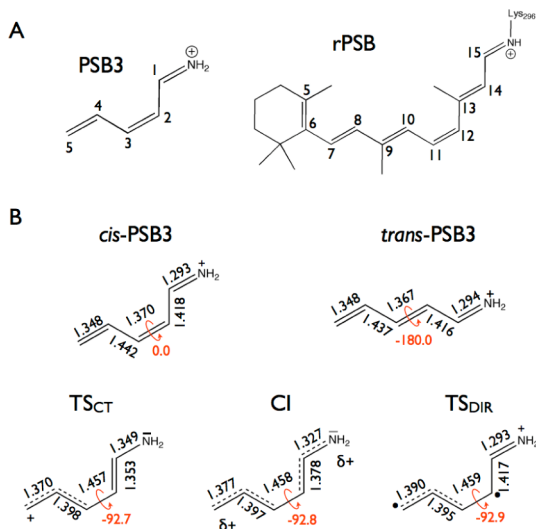
reveal that PSB3 and rPSB exhibit similar features in the first singlet excited state ( $S_1$ ). At the CASSCF level, the  $S_1$  state in both systems features a substantially barrierless potential energy path connecting the Franck–Condon (FC) point to a peaked CI with a ca. 90° twisted central bond,<sup>2,12–14</sup> consistent with the fact that photoisomerization in rhodopsin occurs on a femtosecond time scale.<sup>15–17</sup> Furthermore, vertical excitation at the FC geometry in both models is characterized by a ca. 30–50% charge transfer from one side of the isomerizing double bond to the other (i.e., from the  $\text{NH}_2=\text{C1H}-\text{C2H}=\text{}$  to the  $=\text{C3H}-\text{C4H}=\text{C5H}_2$  fragment in PSB3, and from the  $-\text{C12H}-\text{C13CH}_3=\text{C14H}-\text{C15H}-\text{NH}-$  fragment to the  $\beta$ -ionone-containing moiety in rPSB).<sup>1,12,18</sup> This is because the positive charge, which is almost fully localized on the Schiff base in the ground state ( $S_0$ ), becomes more delocalized along the  $\pi$ -bond framework in the  $S_1$  state.

Received: August 31, 2012

Published: October 22, 2012



**Scheme 1.** (A) The Structures of the 11-*cis*-Retinal Protonated Schiff Base (rPSB) Connected to the Lys296 Residue in Bovine Rhodopsin and Its Reduced Model, the *cis*-Penta-2,4-dieniminium Cation (PSB3) and (B) Selected CASSCF/6-31G\* Geometrical Parameters (Bond Lengths in Ångstroms and C1–C2–C3–C4 Dihedrals in Degrees) for the *cis*-PSB3, *trans*-PSB3, TS<sub>CT</sub>, TS<sub>DIR</sub>, and the CI<sup>a,b</sup>



<sup>a</sup>The resonance formula also provides a qualitative representation of the singlet electron pairing and charge distribution. <sup>b</sup>The CI structure shown is the one intercepted by the Bond Length Alternation (BLA) coordinate.

PSB3 also reproduces several features of the  $S_0$  potential energy surface of opsin-embedded rPSB. In both chromophores, a loop constructed with the branching plane vectors and encompassing the CI passes through regions of different electronic character (see the bottom of Figure 1 and the legend).<sup>19,20</sup> In one region, the molecule has its positive charge fully localized on the Schiff-base-containing moiety, similar to the  $S_0$  reactant (*cis*-PSB3) and the product (*trans*-PSB3); thus, the underlying wave function has predominantly a covalent/diradical character ( $\Psi_{\text{DIR}}$ ). In the other region, the positive charge is almost completely translocated to the other end of the molecule (the allyl group in the case of PSB3, or the  $\beta$ -ionone-containing moiety in the case of rPSB). In this region the wave function is predominantly of charge-transfer character ( $\Psi_{\text{CT}}$ ). A schematic representation of the  $S_0$  energy surface around the CI point is given in Figure 1a. Moreover, in both PSB3<sup>10</sup> and rPSB,<sup>19</sup> each region also hosts a transition state (TS) that could mediate thermal (i.e., proceeding on the ground state) isomerization of the chromophore. One TS (TS<sub>DIR</sub>) lies in the  $\Psi_{\text{DIR}}$  region and, therefore, corresponds to the homolytic cleavage of the isomerizing double bond. The other TS (TS<sub>CT</sub>) is in the  $\Psi_{\text{CT}}$  region and is reached by heterolytic cleavage of the double bond. Both TSs are ca. 90° twisted, similar to the CI, and the main structural difference between TS<sub>DIR</sub>, TS<sub>CT</sub>, and the CI is along the bond length alternation (BLA) coordinate (see Scheme 1B), with the CI situated between the two TSs at the CASSCF level of theory.

The  $S_0$  CASSCF energy surface near the CI of PSB3 was characterized by mapping the surface along three potential energy paths (see Figure 1).<sup>10</sup> The first path (the BLA path) connects the two TSs and intercepts the CI point shown in Scheme 1B. The other two paths are minimum energy paths

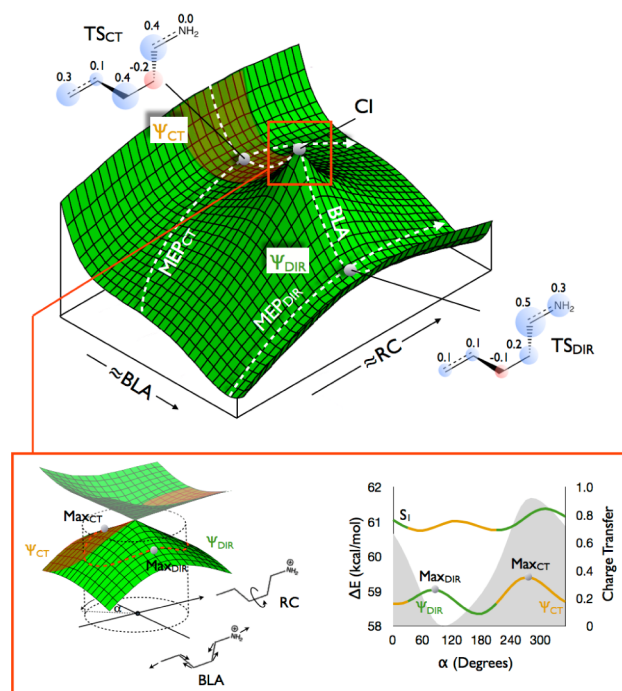


**Figure 1.** Top. Schematic two-dimensional cut of the  $S_0$  potential energy surface of PSB3. The two coordinates can be described as bond length alternation (BLA) and the C2–C3 twisting reaction coordinate (RC), respectively. The region in which the wave function has predominantly a charge-transfer character ( $\Psi_{\text{CT}}$ ) is displayed in brown, whereas the part corresponding to a covalent/diradical wave function ( $\Psi_{\text{DIR}}$ ) is displayed in green. The electronic structure of the two transition states is illustrated by a bubble diagram showing the values of the CASSCF Mulliken charges along the backbone (charges summed onto heavy atoms). The three paths used in the present study (the BLA, MEP<sub>CT</sub>, and MEP<sub>DIR</sub> paths) are shown by dashed lines on the surface. Bottom left. A schematic magnification of the  $S_0/S_1$  CI region. A loop centered around the CI and constructed using the branching plane vectors parallel to the BLA and RC coordinates is shown by the red dashed line on the  $S_0$  surface. The angle  $\alpha$  corresponds to the 0– $2\pi$  coordinate defining the position along the circular loop. Bottom right. The  $S_0$  and  $S_1$  CASSCF energies (colored according to the dominant electronic configuration) as well as the  $S_0$  charge transfer character (gray area) along the angle  $\alpha$  following the loop around the CI. The charge-transfer character is determined by summing the CASSCF Mulliken charges on the allyl (i.e., the  $\text{C}_5\text{H}_2=\text{C}_4\text{H}-\text{C}_3\text{H}-$ ) fragment of the PSB3. The energies and charge transfer character are obtained from ref 10.

(MEPs) connecting *cis*-PSB3 to *trans*-PSB3 through TS<sub>DIR</sub> and TS<sub>CT</sub> (MEP<sub>DIR</sub> and MEP<sub>CT</sub> paths, respectively). The MEP<sub>CT</sub> path, therefore, starts and ends in the  $\Psi_{\text{DIR}}$  regions while intersecting the  $\Psi_{\text{CT}}$  region, whereas the MEP<sub>DIR</sub> path is confined to the  $\Psi_{\text{DIR}}$  region of the  $S_0$  surface (therefore, the molecule maintains a covalent/diradical character in the  $S_0$  state along this path). The two-root SA-CASSCF/6-31G\* energy profiles and the corresponding wave functions along the three paths are shown in Figure 2. Details regarding the generation of these paths are provided in the Methods section.

Owing to the complexity of its potential energy surfaces, sensitivity to the methodology, as well as small molecular size and chemical relevance as a model for rPSB, PSB3 is a useful benchmark system for testing different computational methods. In the present contribution, we extend previous benchmark studies to include single-reference EOM-CC methods.<sup>21–24</sup> The EOM-CC (or linear response CC) methods allow one to

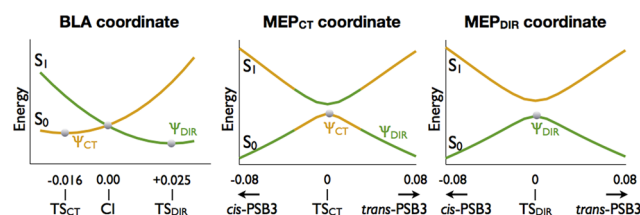


**Figure 2.** The  $S_0$  and  $S_1$  two-root SA-CASSCF/6-31G\* energy profiles along the three paths shown in Figure 1 (BLA,  $\text{MEP}_{\text{CT}}$ , and  $\text{MEP}_{\text{DIR}}$  paths). Regions in which the wave functions are of predominantly charge-transfer character (i.e., with most of the positive charge located on the  $\text{=C3H-C4H=C5H}_2$  fragment) are shown in brown, whereas covalent/diradical regions (i.e., with most of the positive charge located on the  $\text{NH}_2\text{=C1H-C2H=}$  fragment) are green. The BLA coordinate is defined as the difference between the average bond length of the formal single bonds and the formal double bonds (i.e., the difference between the average C2–C1 and C4–C3 bond length and the average C1–N, C3–C2, and C4–C5 bond length).

describe a variety of multiconfigurational wave functions in a strictly single-reference formalism, provided that all leading target configurations are derived by single excitations from the reference. Both dynamical and nondynamical correlation effects are included in a single computational step. The EOM-CC is a multistate approach, that is, multiple electronic states can be computed in one calculation and are described on the same footing (again, provided that all leading configurations are formally single excitations from the reference state).

In EOM-CC, target states,  $\Psi_k = R_k \Phi_0$ , are found as the solutions of a non-Hermitian eigenvalue problem:

$$\bar{H}R_K = E_K R_K \quad \bar{H} = e^{-T} H e^T$$

where  $\bar{H}$  is a similarity transformed Hamiltonian and  $T$  is a general excitation operator satisfying coupled-cluster equations for the reference state ( $\Phi_0$ ).  $\Phi_0$  is a single Slater determinant describing the reference state and is usually (but not always) obtained from a Hartree–Fock calculation. The choice of the excitation operator  $R$  and the reference  $\Phi_0$  is specific for different EOM-CC models;<sup>22</sup> e.g.,  $R$  is a particle-conserving operator in EOM-EE (EOM for excitation energies), a particle-annihilating operator in EOM-IP (EOM ionization potential), a particle-creating operator in EOM-EA (electron attachment EOM), and a spin-flipping (SF) operator in EOM-SF.<sup>25–28</sup>

The excitation level in  $T$  and  $R$  defines a particular EOM-CC model and determines its accuracy and computational cost. Our study employs EOM-CC methods that use operators restricted to the single and double substitutions (with respect to the reference  $\Phi_0$ ), that is, 1h1p + 2h2p (h for hole, p for particle) in  $T$  and in  $R$  (Figure 3 shows the 1h1p part of operator  $R$ ).

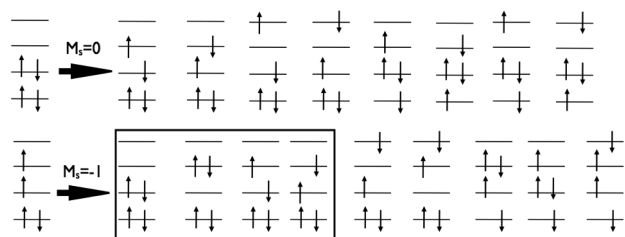


**Figure 3.** Target determinants generated by spin-conserving ( $M_s = 0$ , top) and spin-flipping ( $M_s = -1$ , bottom) excitation operators from singlet ( $M_s = 0$ , top) and triplet ( $M_s = +1$ , bottom) references in the EOM-EE and EOM-SF methods, respectively.

These methods scale as  $N^6$ . To achieve higher accuracy, EOM-CCSD can be augmented by a perturbative account of triple excitations giving rise to EOM-CCSD(dT) or EOM-CCSD(fT) models.<sup>29–31</sup>

Owing to its linear parametrization, the EOM ansatz is capable of describing multiconfigurational wave functions. For example, it can describe two-configurational open-shell excited states for which two determinants are required for spin-adaptation, e.g., for an excited state of a  $\pi\pi^*$  character,  $\Psi_{\text{ex}} \sim |\pi\alpha\pi^*\beta\rangle \pm |\pi\beta\pi^*\alpha\rangle$  ( $\Psi_{\text{DIR}}$  is of that type). Furthermore, states of a mixed character such as  $\pi\pi^*$  mixed with  $n\pi^*$  or Rydberg-type  $\pi 3s(\text{Ry})$  configurations can also be correctly represented by the EOM-EE ansatz.<sup>22,32</sup> However, the limitation of this representation becomes obvious when one considers states of a doubly excited character [e.g.,  $(\pi^*)^2$  in ethylene or dark states in polyenes]—although such doubly excited determinants are present in the EOM-EE-CCSD expansion, they appear at a different excitation level (2h2p), and therefore, states of doubly excited character are not treated on the same footing as singly excited ones. Doubly excited states often become important in the situations when the  $S_0$  wave function acquires multiconfigurational character, e.g., as in diradicals, triradicals, at TSs, isomerization around a double bond, or at CIs.<sup>22,28,33</sup>

The SF approach offers a simple and efficient solution to this sort of electronic structure.<sup>25–28</sup> SF methods employ a high-spin reference state, which is accurately described by a single-reference wave function. For example, in diradicals (or at TSs and along bond-breaking coordinates) where the singlet state HOMO and LUMO (highest occupied and lowest unoccupied molecular orbitals) are (nearly) degenerate, the respective high-spin ( $\alpha\alpha$ ) triplet state is perfectly well behaved as both nearly degenerate orbitals are occupied. The problematic target states, such as closed- and open-shell singlets (and triplets) in diradicals or bond-breaking, are then described as spin-flipping excitations:

$$\Psi_{s,t}(M_s = 0) = R(M_s = -1)\Psi_t(M_s = +1)$$

where  $\Psi_t(M_s = +1)$  is the  $\alpha\alpha$  component of the triplet reference state,  $\Psi_{s,t}(M_s = 0)$  stands for the final singlet and triplet states, respectively, and the operator  $R(M_s = -1)$  is an excitation operator that flips the spin of an electron.

When augmented by triples corrections, either explicitly<sup>34,35</sup> or perturbatively,<sup>30</sup> the respective methods such as EOM(2,3), EOM-SF-CCSD(dT), or EOM-SF-CCSD(fT) allow one to compute relevant energetics (e.g., singlet–triplet or doublet–quartet gaps, potential energy surfaces, etc.) with higher accuracy, often approaching chemical accuracy (e.g., 1 kcal/mol). Triple excitations were also found to be important in EOM-EE calculations (see, for example, refs 36 and 37). EOM-SF calculations do not require active space selection and/or state averaging (thus, EOM excitations and total energies do not depend on the number of states computed). Multiple states can be computed in a single calculation. Since amplitudes of operator  $R$  are obtained by simple diagonalization, changing character of interacting electronic states (i.e., ionic versus covalent) can be correctly described without making any assumptions about dominant character of the wave function. Moreover, exact and near degeneracies and the CIs between the target EOM states can be correctly described<sup>22,38</sup> (but not the CIs between the reference and EOM states.<sup>39</sup> Also, a caveat exists due to a non-Hermitian nature of  $\bar{H}$ <sup>40</sup>). Thus, EOM-SF should be able to tackle changing electronic structures, such as along the BLA,  $\text{MEP}_{\text{CT}}$ , and  $\text{MEP}_{\text{DIR}}$  paths in this work.



A number of benchmark studies exist for EOM-EE-CC on the rhodopsin chromophore and its models, mostly focusing on vertical excitation energies. Send et al. have presented a number of studies of the full gas-phase rPSB chromophore,<sup>41,42</sup> in addition to a benchmark study with reduced model chromophores having varying conjugated chain lengths,<sup>43</sup> where they employed an approximation to EOM-EE-CCSD, the CC2 method, and for smaller models also an EOM model with an approximate account of the triple excitations (CC3). These studies focused on the vertical excitation energy and on the decay path from the FC point and did not investigate the regions near the CI. In one other study,<sup>44</sup> a single point EOM-EE-CCSD energy calculation was performed on the 11-*cis*-retinal, but this is a polyenal and is not the chromophore of visual pigments, which is a protonated Schiff base. Therefore, while different groups have employed EOM-EE-CC methods for studying other biological chromophores such as uracil,<sup>36,45–49</sup> the green fluorescent protein,<sup>50–53</sup> and the photoactive yellow protein,<sup>37,54,55</sup> chromophores, there have been no studies of rPSB models using EOM-CC methods (and in particular EOM-SF). To the best of our knowledge, this is the first such study.

Below, we describe the computational methods used in this study, followed by the presentation of the results and discussion of the EOM-CC energy profiles along the BLA, MEP<sub>CT</sub>, and MEP<sub>DIR</sub> paths. The EOM-CC energy profiles are compared to those of CASSCF, MRCISD, and MRCISD+Q. We find that EOM-SF-CCSD(dT) and EOM-SF-CCSD(fT) are successful in describing the energies of both the  $\Psi_{CT}$  and  $\Psi_{DIR}$  states and yield energy profiles in a nearly quantitative agreement with MRCISD+Q.

## METHODS

This section presents details on the generation of the geometries along the three paths, and on the MRCISD and EOM-CC calculations along these paths. The relevant energies are given in the SI, along with the respective Cartesian coordinates for each path.

**Generation of Path Geometries.** The path geometries used in this study are from ref 10. The paths were generated from the two-root SA-CASSCF/6-31G\* optimized TS<sub>CT</sub> and TS<sub>DIR</sub> structures (shown in Scheme 1B). The active space for these calculations included six electrons and six  $\pi$  orbitals. The BLA path consists of 14 geometries. Those include the TS<sub>CT</sub> structure, the TS<sub>DIR</sub> structure, eight structures obtained by a linear interpolation between the two TSs, and four structures generated by a linear extrapolation of the coordinates (two on the TS<sub>CT</sub> side and two on the TS<sub>DIR</sub> side). As for the MEP<sub>DIR</sub> and MEP<sub>CT</sub> paths, those were generated by running two intrinsic reaction coordinate calculations each from the corresponding TS at the two root SA-CASSCF/6-31G\* level of theory with a step size of 0.01 Å·amu<sup>1/2</sup>. Each of the two MEP paths includes more than 100 geometries, so we do not consider the whole path. The eight structures closest to the transition states from each side are used (thus, each path includes 17 geometries including the transition state). All CASSCF optimization calculations were performed with the Molcas 7.6 software package.<sup>56</sup>

**MRCI Calculations.** The MRCISD and MRCISD+Q energies along the BLA, MEP<sub>CT</sub>, and MEP<sub>DIR</sub> paths are from ref 10. Throughout this work, all energies are reported for the internally contracted (IC) variant of MRCISD and MRCISD+Q with a 6-31G\* basis set and were computed with the

Molpro quantum chemistry package.<sup>57</sup> The IC-MRCISD and uncontracted MRCISD energy profiles have been found to be very similar along the three benchmark paths.<sup>10</sup> The reference space for these calculations included the six electrons and six  $\pi$ -orbitals used to construct the zero-order CASSCF wave functions. The 1s core orbitals of carbon and nitrogen were kept frozen. In MRCISD+Q, the Davidson correction<sup>58</sup> with a relaxed reference<sup>59</sup> was used; this eliminates kinks around CI observed for the original Davidson correction (see Figure S1).

**EOM-CC Calculations.** Calculations were performed with the 6-31G\* basis set using Cartesian d-functions, consistent with the CASSCF and MRCISD calculations. All electrons were correlated in the CCSD and EOM calculations. In EOM-EE, the lowest closed-shell Hartree–Fock solution was used as the reference. In EOM-SF, the lowest high-spin triplet was employed as the reference. The quality of the EOM-SF wave functions can be affected by spin-contamination; this can be mitigated by employing a ROHF triplet reference. Thus, for highest-accuracy SF results using ROHF is recommended; however, if the UHF solution is not strongly spin-contaminated, it can also be used. We present both UHF and ROHF based EOM-SF-CCSD results. The  $\langle S^2 \rangle$  values of the target EOM-SF wave functions present a reliable diagnostic of spin-contamination. For PSB3, the spin-contamination of the UHF triplet reference is too large, spoiling the description of the target states. For example, at the TS<sub>CT</sub> geometry, the  $\langle S^2 \rangle$  values of the three lowest EOM-SF/UHF states are 0.87 (open-shell singlet corresponding to  $\Psi_{dir}$ ), 1.24 ( $M_s = 0$  triplet), and 0.07 (closed-shell singlet, ionic state  $\Psi_{CT}$ ), whereas using the ROHF reference, the  $\langle S^2 \rangle$  values become much closer to the spin-pure values (0.012, 2.026, and 0.063). All EOM-CC calculations were performed using the Q-Chem electronic structure package.<sup>60</sup>

The degree of charge transfer (see also Figure 1 legend) along the investigated paths is quantified by computing the sum of Mulliken charges on the =C3H–C4H=C5H<sub>2</sub> fragment. This goes from near 0.0 to 1.0 when moving from a fully diradical (e.g., as in TS<sub>DIR</sub>) to a fully charge transfer (e.g., as in TS<sub>CT</sub>) character of the wave function respectively.

## RESULTS AND DISCUSSION

Here, we systematically describe and compare the shapes of the potential energy profiles along the BLA, MEP<sub>CT</sub>, and MEP<sub>DIR</sub> coordinates computed with the CASSCF, MRCISD/MRCISD+Q, and EOM-CC methods.

**BLA Path.** The  $S_0$  and  $S_1$  energies computed with various EOM-CC methods are compared to those of CASSCF, MRCISD, and MRCISD+Q in Figure 4. We assume that MRCISD+Q provides the highest-quality potential energy surfaces. We note that the CASSCF curves are quite different, signifying the importance of dynamical correlation. MRCISD+Q yields the  $\Psi_{CT}$  curve with a minimum (corresponding to TS<sub>CT</sub>) that is more stable than the  $\Psi_{DIR}$  curve minimum (corresponding to TS<sub>DIR</sub>). Moreover, at the MRCISD+Q level, TS<sub>DIR</sub> becomes an excited-state minimum along the BLA coordinate rather than a true TS, while the CI becomes intermediate/sloped.<sup>61</sup>

Below, we will discuss the effect of the various methods on the relative stabilities of the  $\Psi_{CT}$  and  $\Psi_{DIR}$  curves along the BLA coordinate. To better quantify this effect, we report (Table 1) the  $S_0$ – $S_1$  energy gap at the TS<sub>DIR</sub> and TS<sub>CT</sub> geometries, to complement the information shown in Figure 4. To provide additional measure of the discrepancies between different

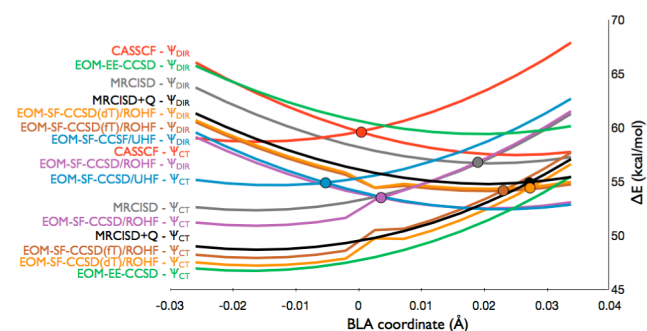


**Figure 4.** The  $S_0$  and  $S_1$  energy profiles along the BLA coordinate. The methods displayed are EOM-EE-CCSD (green), EOM-SF-CCSD/UHF (blue), EOM-SF-CCSD/ROHF (violet), EOM-SF-CCSD(dT)/ROHF (orange), EOM-SF-CCSD(fT)/ROHF (brown), uncorrected MRCISD (gray), and MRCISD+Q (black), along with CASSCF (red). The energy values are relative to the reactant (*cis*-PSB3). The position of the CI for each method is indicated with a filled circle. The curves are labeled on the left to distinguish between the diabatic curves with ionic/charge transfer ( $\Psi_{CT}$ ) character and the covalent/diradical ( $\Psi_{DIR}$ ) character for each method.

methods, we also report the NPE (nonparallelity errors, see Table 1 legend) values along the three paths for different methods relative to the MRCISD+Q curves. The NPEs quantify how different the shapes of PESs are, i.e., zero NPE corresponds to the identical-shape surfaces (note that NPE does not say anything about the relative positions of the two surfaces).

As Figure 4 illustrates, EOM-EE-CCSD yields potential energy curves that have correct shapes. The NPEs relative to MRCISD+Q are 0.4 and 0.3 kcal/mol for the  $\Psi_{CT}$  and  $\Psi_{DIR}$ , respectively. This is not surprising, as the analysis of the EOM-SF wave function amplitudes (below) confirms essentially single-configurational character of  $\Psi_{CT}$ , which is dominated by the closed-shell determinant at all BLA values (the leading EOM-SF amplitude corresponding to this configuration is 0.86–0.94 along the scan). Thus, the CCSD wave function is qualitatively correct for  $\Psi_{CT}$ , and the open-shell diradical state,  $\Psi_{DIR}$ , can be correctly described by EOM (see Figure 3). However, the two curves are considerably shifted with respect to each other; i.e., the  $\Psi_{CT}$  curve is overstabilized and the  $\Psi_{DIR}$  curve is destabilized (the gap between the two states at  $TS_{CT}$  is 16.6 kcal/mol, to be compared to the MRCISD+Q value of

10.2 kcal/mol). As a result, the EOM-EE-CCSD CI is shifted to a much larger BLA value and does not even appear within the selected BLA coordinate values shown in Figure 4. Using a polynomial fit to extrapolate the curves (see Figure S2) yields a EOM-EE-CCSD CI that has a BLA value of 0.052 Å. This is expected, as EOM-EE treats the two states on a different footing; i.e.,  $\Psi_{CT}$  as the reference and  $\Psi_{DIR}$  as an EOM state. Consequently, EOM-EE fails to describe the degeneracy between the two states correctly.

The description of the relative position of the two states is improved when using the SF approach. EOM-SF-CCSD/UHF yields the  $\Psi_{DIR}$  curve that is only slightly overstabilized with respect to MRCISD+Q, and the  $\Psi_{CT}$  curve that is not stable enough, thus shifting the CI geometry to the BLA value of ca.  $-0.005$  Å, which is too low compared to that of the MRCISD+Q CI (the BLA value of ca. 0.030 Ångstroms).

Next, we investigate the effect of reducing spin-contamination in EOM-SF-CCSD by employing a ROHF reference. Consistently with large EOM-SF-CCSD/UHF spin-contamination (see the Methods section above), we observe a noticeable change in the curves. Whereas the effect on the  $\Psi_{DIR}$  curve is small, reducing spin-contamination does stabilize the  $\Psi_{CT}$  curve and, therefore, brings it closer to the MRCISD+Q  $\Psi_{CT}$  one. Consequently, this also moves the CI geometry toward that of MRCISD+Q.

Interestingly, we observe a kink on the EOM-SF-CCSD/ROHF BLA energy profile near 0.00 Å of the BLA coordinate, that is, near the CI. The analysis of the SF wave function of the  $\Psi_{CT}$  state reveals that the discontinuity is correlated with the changes in the wave function composition. As shown in Figure S3, the leading coefficient in the  $\Psi_{CT}$  wave function, which corresponds to the closed-shell determinant, smoothly changes from 0.86 to 0.95 along the BLA scan except for the point at 0.00 Å where it drops to 0.84 (thus, the share of the diradical configurations in the wave function increases). This change in the wave function is also responsible for the large NPE for  $\Psi_{CT}$  (see Table 1 and Figure S4). Note that the character of the triplet reference state varies smoothly, and the respective curves (ROHF, CCSD, and EOM-SF-CCSD, see Figure S5) have no kinks. We note that the computed energies correspond to the adiabatic states, and the diabatic (i.e.,  $\Psi_{CT}$  and  $\Psi_{DIR}$ ) curves are drawn by simply connecting the dots following the leading character of the adiabatic wave functions. Thus, the discontinuity of the so-drawn diabatic curves should disappear

**Table 1.** The  $S_0$ – $S_1$  Energy Gaps ( $\Delta E$ , kcal/mol) at  $TS_{CT}$ ,  $TS_{DIR}$ , and *cis*-PSB3, As Well As the Nonparallelity Errors (NPEs, kcal/mol) along the BLA,  $MEP_{CT}$ , and  $MEP_{DIR}$  Paths for Various Methods Examined in This Study<sup>a</sup>

method	$\Delta E$ at $TS_{CT}$	$\Delta E$ at $TS_{DIR}$	$\Delta E$ at <i>cis</i> -PSB3	BLA		$MEP_{CT}$		$MEP_{DIR}$	
				NPE along $\Psi_{CT}$ curve	NPE along $\Psi_{DIR}$ curve	$S_0$ NPE	$S_1$ NPE	$S_0$ NPE	$S_1$ NPE
MRCISD+Q	10.2	0.6	101.4						
MRCISD	8.8	<b>1.6</b>	104.8	0.6	0.6	1.7	1.3	0.6	0.4
CASSCF	4.5	7.4	110.3	0.8	2.4	5.6	4.3	2.3	2.3
EE-CCSD/UHF	16.6	6.9		0.4	0.3				
SF-CCSD/UHF	2.4	7.5		0.5	0.8				
SF-CCSD/ROHF	5.8	<b>6.0</b>	105.5	2.2 (2.2)	0.2 (0.1)	3.3	2.9	1.8	3.2
SF-CCSD(dT)/ROHF	11.1	0.6	102.1	1.4 (1.0)	0.9 (0.2)	0.4	0.4	1.3	0.8
SF-CCSD(fT)/ROHF	10.2	<b>0.6</b>		1.5 (1.4)	0.7 (0.2)				

<sup>a</sup>MRCISD+Q is our reference method against which all NPEs are computed. Energy gaps reported in bold have a different order of states with respect to MRCISD+Q at the  $TS_{DIR}$  geometry. NPEs were computed along the entire BLA path of Figure 4, and along a section (ranging from  $-0.08$  to  $0.08$  Å·amu<sup>1/2</sup>) of the  $MEP_{CT}$  and  $MEP_{DIR}$  paths. Values reported in parentheses are NPEs calculated when ignoring the kinks along the BLA energy profile, which are discussed in the Results and Discussion section on the BLA path.

if proper diabaticization is performed. A similar behavior is observed in the MRCISD wave functions, giving rise to the kinks in MRCISD(+Q) curves around the MRCISD CI, as illustrated in Figure S1. This problem is rectified by “rotating” the MR-CISD states, which is exploited in the modified Davidson correction;<sup>59</sup> a similar procedure could be used within the EOM-SF-CCSD formalism.

Finally, we investigate the effect of including the correction due to triple excitations in EOM-SF-CCSD. The two corrections, denoted as (dT) and (fT), are derived by using second-order Rayleigh–Schroedinger perturbation theory starting from the EOM-SF-CCSD solutions as zero-order states.<sup>30</sup> The difference between the two corrections is in the definition of the triples–triples block of  $H_0$ . In (dT), the diagonal of the full similarity transformed Hamiltonian is employed, whereas in (fT) the Fock matrix (i.e., orbital energy differences) is used. We consider (dT) to be superior. In previous benchmark studies,<sup>30,31</sup> the performance of both corrections was found to be similar.

The inclusion of triples correction leads, as expected, to a further stabilization of the  $\Psi_{CT}$  curve and, therefore, to a better agreement with the MRCISD+Q energy profile. Both the EOM-SF-CCSD(dT)/ROHF and EOM-SF-CCSD(fT)/ROHF BLA energy profiles of Figure 4 are effectively reproducing the MRCISD+Q result, with both the  $\Psi_{CT}$  and  $\Psi_{DIR}$  curves being only slightly lower in energy. However, we note that the artifact from the EOM-SF-CCSD/ROHF calculations persists. There is a clear discontinuity in the BLA energy profile occurring near the BLA coordinate of 0.00 Å for all three EOM-SF/ROHF methods (see also Figure S4). This is expected as the discontinuity originates in the mixing of the zero-order wave functions of the two diabatic states near the CI. In such situations, it would be more appropriate to apply perturbation theory for the degenerate states, rather than follow nondegenerate formalism as was done in deriving (dT) and (fT) triples corrections.<sup>30,31</sup>

Since this kink also corresponds to the change in the wave function composition, we note that the triple excitation correction curves behave slightly differently before and after the kink. At negative BLA values (before the kink), the EOM-SF-CCSD(fT)/ROHF profile is in better agreement with MRCISD+Q, as indicated by the agreement of the  $S_0$ – $S_1$  energy gap at the  $TS_{CT}$  geometry, while EOM-SF-CCSD(dT)/ROHF slightly overstabilizes the  $\Psi_{CT}$  state, yielding a larger gap. However, at positive BLA values (after the kink), we find that EOM-SF-CCSD(dT)/ROHF is in better agreement with MRCISD+Q, as indicated by the energy gap at  $TS_{DIR}$  and the similar position of the CI in Figure 4. On the other hand, EOM-SF-CCSD(fT)/ROHF reverses the state ordering at the  $TS_{DIR}$  geometry and shifts the CI toward lower BLA values with respect to MRCISD+Q. These differences appear to fall within 1–2 kcal/mol and yield a difference in the position of the crossing of ca. 0.005 Å.

**MEP<sub>CT</sub> Path.** Figure 5A presents the  $S_0$  and  $S_1$  EOM-SF-CCSD/ROHF and EOM-SF-CCSD(dT)/ROHF energies along the MEP<sub>CT</sub> path and compares them to CASSCF, MRCISD, and MRCISD+Q. The energies at 0 Å of the MEP<sub>CT</sub> path are identical to the point at –0.016 Å along the BLA coordinate since they correspond to the same geometry ( $TS_{CT}$ , where the two paths cross). At the  $TS_{CT}$  geometry, the  $S_0$  state is of  $\Psi_{CT}$  character, whereas  $S_1$  is  $\Psi_{DIR}$ . As we move away from  $TS_{CT}$  along the MEP<sub>CT</sub> path either toward the reactant or the product, we find that the  $S_0$  wave function gradually loses its

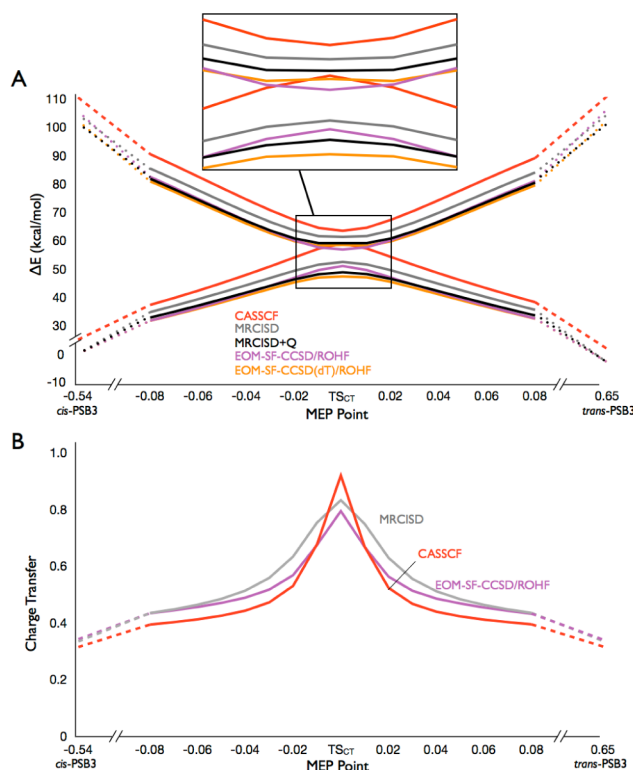


**Figure 5.** Energy profiles along the MEP<sub>CT</sub> coordinate. (A) The  $S_0$  and  $S_1$  energies computed using EOM-SF-CCSD/ROHF (violet), EOM-SF-CCSD(dT)/ROHF (orange), uncorrected MRCISD (gray), MRCISD+Q (black), and CASSCF (red). The energies are relative to the reactant (*cis*-PSB3, –0.54 Å). The region defined by –0.02 to 0.02 Å is magnified in the inset. (B) The charge-transfer character of the  $S_0$  state along MEP<sub>CT</sub> for CASSCF (red), uncorrected MRCISD (gray), and EOM-SF-CCSD/ROHF (violet). See Figure 1 caption and the Methods section for an explanation on how the charge transfer character is determined.

charge-transfer character and becomes more mixed with the diradical configurations (see Figure 5B). Conversely, this is also true for the  $S_1$  state which loses its diradical character and gains a partial charge-transfer character along the same path.<sup>60</sup> In light of this, the shape of the EOM-SF-CCSD/ROHF energy profile along MEP<sub>CT</sub> can be rationalized by the tendency of this method to overstabilize the  $\Psi_{DIR}$  wave functions with respect to  $\Psi_{CT}$ . At the *cis*-PSB3 and *trans*-PSB3 geometries, where the  $S_0$  state is  $\Psi_{DIR}$  and the  $S_1$  state is  $\Psi_{CT}$ , we find that EOM-SF-CCSD/ROHF overestimates the  $S_0$ – $S_1$  energy gap, as compared to MRCISD+Q (see the  $S_0$ – $S_1$  gaps reported in Table 1). Meanwhile, at the  $TS_{CT}$  geometry, where the  $S_0$  state is  $\Psi_{CT}$  and  $S_1$  is  $\Psi_{DIR}$ , EOM-SF-CCSD/ROHF underestimates the  $S_0$ – $S_1$  energy gap (also see Table 1). This change in wave function along the MEP<sub>CT</sub> path is responsible for the large NPE for EOM-SF-CCSD/ROHF (NPEs of 3.3 and 2.9 kcal/mol for  $S_0$  and  $S_1$ , respectively).

On the other hand, the EOM-SF-CCSD(dT)/ROHF method yields the MEP<sub>CT</sub> profile that is much more similar to MRCISD+Q (NPEs of 0.4 kcal/mol for both  $S_0$  and  $S_1$ ); however, it has consistently lower  $S_0$  and  $S_1$  energies for the nonplanar structures (i.e., structures along the –0.08 to +0.08 Å range of the MEP<sub>CT</sub> path). In the case of planar structures (*cis* and *trans*-PSB3), the EOM-SF-CCSD(dT)/ROHF  $S_0$  and  $S_1$  relative energies agree quantitatively with MRCISD+Q (for *cis*-



PSB3: 102.1 kcal/mol compared to 101.4 kcal/mol, respectively).

Figure 5B illustrates the EOM-SF-CCSD/ROHF  $S_0$  charge-transfer character along the MEP<sub>CT</sub> path. We find that at the TS<sub>CT</sub> geometry,  $S_0$  has slightly less charge-transfer character than it does at the CASSCF and MRCISD levels. Moreover, we find that the EOM-SF-CCSD/ROHF charge transfer profile is intermediate between that of CASSCF and MRCISD. This is consistent with the observation that EOM-SF-CCSD/ROHF stabilizes  $\Psi_{CT}$  more than  $\Psi_{DIR}$  compared to CASSCF, but not as much as MRCISD, and therefore has an intermediate extension of the charge transfer region.

**MEP<sub>DIR</sub> Path.** The  $S_0$  and  $S_1$  EOM-SF-CCSD/ROHF and EOM-SF-CCSD(dT)/ROHF energies along the MEP<sub>DIR</sub> path are presented in Figure 6A along with the CASSCF, MRCISD,

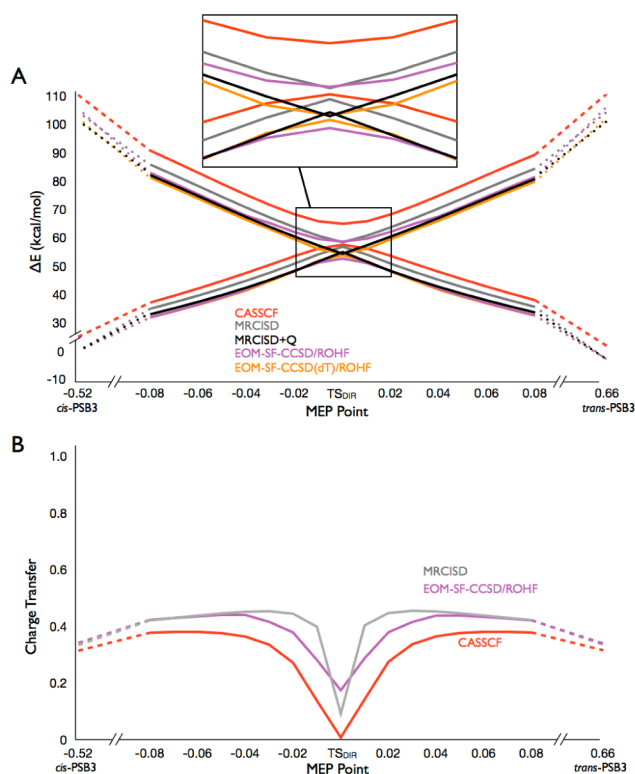


**Figure 6.** Energy profiles along the MEP<sub>DIR</sub> coordinate. (A) The  $S_0$  and  $S_1$  energies computed using EOM-SF-CCSD/ROHF (violet), EOM-SF-CCSD(dT)/ROHF (orange), uncorrected MRCISD (gray), MRCISD+Q (black), and CASSCF (red). The energies are relative to the reactant (*cis*-PSB3,  $-0.52$  Å). The inset magnifies the region from  $-0.02$  to  $0.02$  Å. (B) The charge-transfer character of the  $S_0$  state along MEP<sub>DIR</sub> for CASSCF (red), uncorrected MRCISD (gray), and EOM-SF-CCSD/ROHF (violet). See Figure 1 caption and the Methods section for an explanation on how the charge transfer character is determined.

and MRCISD+Q energies. Along this scan, the point at  $0.00$  Å of the MEP<sub>DIR</sub> path corresponds to TS<sub>DIR</sub> and is identical to the point at around  $0.025$  Å of the BLA coordinate. At the MRCISD and EOM-SF-CCSD/ROHF levels of theory, the entire  $S_0$  state along this path is described by a  $\Psi_{DIR}$  wave function, whereas the  $S_1$  state is  $\Psi_{CT}$ . As a result, we find that EOM-SF-CCSD/ROHF uniformly overstabilizes the  $S_0$  state and destabilizes the  $S_1$  state at the *cis*-PSB3, TS<sub>DIR</sub>, and *trans*-PSB3 geometries with respect to MRCISD+Q, leading consistently to an overestimated  $S_0$ – $S_1$  energy gap (by ca. 5

kcal/mol at both the equilibrium structures and at TS<sub>DIR</sub>). However, along the path connecting the TS to the reactant and product, there is an agreement between the EOM-SF-CCSD/ROHF and MRCISD+Q  $S_1$  energy profiles along both the MEP<sub>CT</sub> (Figure 5A) and MEP<sub>DIR</sub> (Figure 6A) paths. The NPE for EOM-SF-CCSD/ROHF along the MEP<sub>DIR</sub> path is 1.8 and 3.2 kcal/mol for  $S_0$  and  $S_1$ , respectively.

As for the EOM-SF-CCSD(dT)/ROHF energy profile along the MEP<sub>DIR</sub> path (Figure 6A), we find, again, that it is in good agreement with MRCISD+Q but (consistently with the results shown in Figures 4 and 5A) is lower in energy along the entire path (NPE error is 1.3 and 0.8 kcal/mol for  $S_0$  and  $S_1$ , respectively). As shown in the inset of Figure 6A, the TS<sub>DIR</sub> geometry is very close to the CI (i.e., the two states are almost degenerate), and in fact, the  $S_0$  state is of  $\Psi_{CT}$  character at both the EOM-SF/CCSD(dT)/ROHF and MRCISD+Q levels of theory (this is clear in Figure 4).

Finally, in Figure 6B we show the EOM-SF-CCSD/ROHF  $S_0$  charge-transfer character along the MEP<sub>DIR</sub> path where we find that at the TS<sub>DIR</sub> geometry, the wave function has slightly less diradical character (i.e., more charge-transfer character) than it does at the CASSCF and MRCISD levels. Here, the extension of the diradical region shrinks compared to CASSCF as a result of the stabilization/increase in extension of the charge transfer region, but again not to the same extent as MRCISD.

## CONCLUSIONS AND PERSPECTIVES

The results presented in this work reinforce the conclusions of the recent MRPT2 benchmark study<sup>10</sup> that dynamical electron correlation is crucially important for the accurate description of the two lowest electronic states of PSB3 near the CI. Similarly to MRCISD, the dynamical correlation appears to be more important for the state with ionic (i.e., CT) character for EOM-CC methods as well. Perturbative inclusion of triple excitations on top of the EOM-SF-CCSD wave functions stabilizes the charge transfer ( $\Psi_{CT}$ ) regions with respect to the diradical ( $\Psi_{DIR}$ ) regions. Indeed, we note that EOM-SF-CCSD(dT)/ROHF yields a flatter region on the  $S_0$  potential energy surface where the wave function is  $\Psi_{CT}$ , and the topology of the CI changes from peaked to intermediate/sloped. This may have important implications for the photochemistry of such systems and, as recently demonstrated, also for their thermal reactivities with an obvious impact on our understanding of the way visual pigments function.<sup>19</sup>

Our results indicate that single-reference EOM-CC methods are capable of describing the relevant areas of the PSB3  $S_0$  potential energy surface and underlying wave functions with quantitative accuracy when the SF approach is employed and when second-order perturbative corrections are included incorporating the effect of triple excitations.

The EOM-EE-CCSD method yields qualitatively correct diabatic wave functions and potential energy profiles that are nearly parallel to MRCISD+Q (NPEs of 0.4 and 0.3 kcal/mol for  $\Psi_{CT}$  and  $\Psi_{DIR}$ , respectively); however, because the two states are not described on an equal footing (one is the reference, and another—an EOM state), the relative positions of the two curves are not well reproduced (the gap between the two states is overestimated by about 6.4 kcal/mol). Consequently, the position of the CI is shifted. Nevertheless, one may employ EOM-EE-CCSD for generating potential energy surfaces of the two states that need to be offset by using higher-level calculations of the relative state energies.

The EOM-SF-CCSD method, which treats both states on an equal footing as spin-flipping excitations from the high-spin triplet reference, yields potential energy profiles which are in much better agreement with MRCISD+Q. Because both the  $S_0$  and  $S_1$  states are EOM target states, EOM-SF is better suited to describe the CI between these states, in contrast to EOM-EE. Perturbative inclusion of triple excitations results in energy profiles which are in quantitative agreement with MRCISD+Q. We note that using ROHF references in the SF calculations is important for mitigating spin-contamination. In sum, although the SF approach is not designed to describe global potential energy surfaces involving breaking an arbitrary number of bonds, it is capable of treating extended areas of the potential energy surfaces involving isomerization around double bonds, as in the model retinal system considered here. Owing to the robust black-box nature of single-reference EOM-SF-CCSD, which does not involve active space selection and state-averaging, this methodology presents an attractive alternative to multireference approaches. The computational scaling of EOM-SF-CCSD and EOM-SF-CCSD(dT) is  $N^6$  and  $N^7$ , respectively. We note that there are small discontinuities in the pseudodiabatic curves computed by EOM-SF-CCSD in the vicinity of the CIs. These discontinuities may be eliminated by rigorous diabaticization, similarly to the procedure employed in calculating Davidson correction for nearly degenerate MRCISD states. Our results suggest that reformulation of perturbative triples corrections for EOM methods using degenerate perturbation theory formalism is highly desirable for describing conical intersections. Finally, for practical applications of EOM-SF-CCSD(dT) in modeling photochemical reactions, analytic gradients and properties calculations need to be developed and implemented.

## ■ ASSOCIATED CONTENT

### Supporting Information

Five Supporting Figures showing a comparison of MRCISD energies with original Davidson and relaxed reference Davidson corrections, a polynomial fit of the EOM-EE-CCSD BLA curves, energies of the triplet reference state, and additional information on the EOM-SF-CCSD discontinuity and errors against MRCISD+Q. Coordinates and energies for all structures along the BLA, MEP<sub>CT</sub>, and MEP<sub>DIR</sub> paths. This material is available free of charge via the Internet at <http://pubs.acs.org/>.

## ■ AUTHOR INFORMATION

### Corresponding Author

\*E-mail: krylov@usc.edu, molivuc@bgnet.bgsu.edu.

### Notes

The authors declare no competing financial interest.

## ■ ACKNOWLEDGMENTS

We thank Prof. John F. Stanton for insightful remarks and critical suggestions. This work was supported by the Bowling Green State University. M.O. is grateful to the Center for Photochemical Sciences of Bowling Green State University for startup funds. M.O. is also grateful to the National Science Foundation for the CHE-1152070 grant. We are grateful to the Ohio Supercomputer Center and NSF-TeraGrid for granted computer time for multireference calculations. Most of the EOM-CCSD calculations were performed on a Mac laptop. A.I.K. acknowledges support from the National Science

Foundation through the CHE-0951634 grant and from the Humboldt Research Foundation (Bessel Award). A.I.K. is deeply indebted to the Dornsife College of Letters, Arts, and Sciences and the WISE program (USC) for bridge funding support.

## ■ REFERENCES

- (1) Garavelli, M.; Celani, P.; Bernardi, F.; Robb, M. A.; Olivucci, M. J. *Am. Chem. Soc.* **1997**, *119*, 6891–901.
- (2) Garavelli, M.; Bernardi, F.; Robb, M. A.; Olivucci, M. J. *Mol. Struct.: THEOCHEM* **1999**, *463*, 59–64.
- (3) Page, C. S.; Olivucci, M. J. *Comput. Chem.* **2003**, *24*, 298–309.
- (4) Sinicropi, A.; Migani, A.; De Vico, L.; Olivucci, M. *Photochem. Photobiol. Sci.* **2003**, *2*, 1250–5.
- (5) Fantacci, S.; Migani, A.; Olivucci, M. J. *Phys. Chem. A* **2004**, *108*, 1208–13.
- (6) Barbatti, M.; Ruckebauer, M.; Szymczak, J. J.; Aquino, A. J.; Lischka, H. *Phys. Chem. Chem. Phys.* **2008**, *10*, 482–94.
- (7) Valsson, O.; Filippi, C. J. *Chem. Theory Comput.* **2010**, *6*, 1275–1292.
- (8) Mori, T.; Nakano, K.; Kato, S. J. *Chem. Phys.* **2010**, *133*, 064107.
- (9) Coccia, E.; Guidoni, L. J. *Comput. Chem.* **2012**, *33*, 2332–9.
- (10) Gozem, S.; Huntress, M.; Schapiro, I.; Lindh, R.; Granovsky, A. A.; Angeli, C.; Olivucci, M. J. *Chem. Theory Comput.* **2012**, article ASAP.
- (11) Ferré, N.; Olivucci, M. J. *Am. Chem. Soc.* **2003**, *125*, 6868–9.
- (12) Frutos, L. M.; Andrúniów, T.; Santoro, F.; Ferré, N.; Olivucci, M. *Proc. Natl. Acad. Sci. U. S. A.* **2007**, *104*, 7764–9.
- (13) Tomasello, G.; Olaso-González, G.; Altoè, P.; Stenta, M.; Serrano-Andrés, L.; Merchán, M.; Orlandi, G.; Bottoni, A.; Garavelli, M. J. *Am. Chem. Soc.* **2009**, *131*, 5172–86.
- (14) Laricheva, E. N.; Gozem, S.; Rinaldi, S.; Melaccio, F.; Valentini, A.; Olivucci, M. J. *Chem. Theory Comput.* **2012**, *8*, 2559–63.
- (15) Schoenlein, R. W.; Peteanu, L. A.; Mathies, R. A.; Shank, C. V. *Science* **1991**, *254*, 412–5.
- (16) Kandori, H.; Furutani, Y.; Nishimura, S.; Shichida, Y.; Chosrowjan, H.; Shibata, Y.; Mataga, N. *Chem. Phys. Lett.* **2001**, *334*, 271–6.
- (17) Kukura, P.; McCamant, D. W.; Yoon, S.; Wandschneider, D. B.; Mathies, R. A. *Science* **2005**, *310*, 1006–9.
- (18) Strambi, A.; Coto, P. B.; Ferré, N.; Olivucci, M. *Theor. Chem. Acc.* **2007**, *118*, 185–91.
- (19) Gozem, S.; Schapiro, I.; Ferré, N.; Olivucci, M. *Science* **2012**, *337*, 1225–8.
- (20) Coto, P. B.; Sinicropi, A.; De Vico, L.; Ferré, N.; Olivucci, M. *Mol. Phys.* **2006**, *104*, 983–91.
- (21) Stanton, J. F.; Gauss, J. In *Adv. Chem. Phys.*; Prigogine, I. Rice, S. A., Ed.; John Wiley & Sons, Inc.: New York, 2003; Vol. 125, pp 101–146.
- (22) Krylov, A. I. *Annu. Rev. Phys. Chem.* **2008**, *59*, 433–62.
- (23) Sneskov, K.; Christiansen, O. *WIREs Comput. Mol. Sci.* **2011**, *2*, 566–84.
- (24) Bartlett, R. J. *WIREs Comput. Mol. Sci.* **2012**, *2*, 126–38.
- (25) Krylov, A. I. *Chem. Phys. Lett.* **2001**, *338*, 375–84.
- (26) Slipchenko, L. V.; Krylov, A. I. J. *Chem. Phys.* **2002**, *117*, 4694.
- (27) Levchenko, S. V.; Krylov, A. I. J. *Chem. Phys.* **2004**, *120*, 175–85.
- (28) Krylov, A. I. *Acc. Chem. Res.* **2006**, *39*, 83–91.
- (29) Piecuch, P.; Włoch, M. J. *Chem. Phys.* **2005**, *123*, 224105.
- (30) Manohar, P. U.; Krylov, A. I. J. *Chem. Phys.* **2008**, *129*, 194105.
- (31) Manohar, P. U.; Stanton, J. F.; Krylov, A. I. J. *Chem. Phys.* **2009**, *131*, 114112.
- (32) Reisler, H.; Krylov, A. I. *Int. Rev. Phys. Chem.* **2009**, *28*, 267–308.
- (33) Krylov, A. I. J. *Phys. Chem. A* **2005**, *109*, 10638–45.
- (34) Slipchenko, L. V.; Krylov, A. I. J. *Chem. Phys.* **2005**, *123*, 084107.
- (35) Golubeva, A. A.; Nemukhin, A. V.; Klippenstein, S. J.; Harding, L. B.; Krylov, A. I. J. *Phys. Chem. A* **2007**, *111*, 13264–71.



- (36) Epifanovsky, E.; Kowalski, K.; Fan, P. D.; Valiev, M.; Matsika, S.; Krylov, A. I. *J. Phys. Chem. A* **2008**, *112*, 9983–92.
- (37) Zuev, D.; Bravaya, K. B.; Crawford, T. D.; Lindh, R.; Krylov, A. I. *J. Chem. Phys.* **2011**, *134*, 034310.
- (38) Stanton, J. F. *J. Chem. Phys.* **2001**, *115*, 10382.
- (39) Ben-Nun, M.; Quenneville, J.; Martínez, T. J. *J. Phys. Chem. A* **2000**, *104*, 5161–75.
- (40) Köhn, A.; Tajti, A. *J. Chem. Phys.* **2007**, *127*, 044105.
- (41) Send, R.; Sundholm, D. *Phys. Chem. Chem. Phys.* **2007**, *9*, 2862–7.
- (42) Send, R.; Kaila, V. R. I.; Sundholm, D. *J. Chem. Theory Comput.* **2011**.
- (43) Send, R.; Sundholm, D.; Johansson, M. P.; Pawłowski, F. *J. Chem. Theory Comput.* **2009**, *5*, 2401–2414.
- (44) Trabanino, R. J.; Vaidehi, N.; Goddard, W. A. *J. Phys. Chem. B* **2006**, *110*, 17230–9.
- (45) Golubeva, A. A.; Krylov, A. I. *Phys. Chem. Chem. Phys.* **2009**, *11*, 1303–11.
- (46) Khistyayev, K.; Bravaya, K. B.; Kamarchik, E.; Kostko, O.; Ahmed, M.; Krylov, A. I. *Faraday Discuss.* **2011**, *150*, 313–30; discussion 391–418.
- (47) Ghosh, D.; Isayev, O.; Slipchenko, L. V.; Krylov, A. I. *J. Phys. Chem. A* **2011**, *115*, 6028–38.
- (48) Bravaya, K. B.; Kostko, O.; Ahmed, M.; Krylov, A. I. *Phys. Chem. Chem. Phys.* **2010**, *12*, 2292–307.
- (49) Kostko, O.; Bravaya, K.; Krylov, A.; Ahmed, M. *Phys. Chem. Chem. Phys.* **2010**, *12*, 2860–72.
- (50) Epifanovsky, E.; Polyakov, I.; Grigorenko, B.; Nemukhin, A.; Krylov, A. I. *J. Chem. Theory Comput.* **2009**, *5*, 1895–906.
- (51) Polyakov, I. V.; Grigorenko, B. L.; Epifanovsky, E. M.; Krylov, A. I.; Nemukhin, A. V. *J. Chem. Theory Comput.* **2010**.
- (52) Epifanovsky, E.; Polyakov, I.; Grigorenko, B.; Nemukhin, A.; Krylov, A. I. *J. Chem. Phys.* **2010**, *132*, 115104.
- (53) Kowalski, K.; Krishnamoorthy, S.; Villa, O.; Hammond, J. R.; Govind, N. *J. Chem. Phys.* **2010**, *132*, 154103.
- (54) Zuev, D.; Bravaya, K. B.; Makarova, M. V.; Krylov, A. I. *J. Chem. Phys.* **2011**, *135*, 194304.
- (55) Gromov, E. V.; Burghardt, I.; Köppel, H.; Cederbaum, L. S. *J. Am. Chem. Soc.* **2007**, *129*, 6798–806.
- (56) Aquilante, F.; De Vico, L.; Ferré, N.; Ghigo, G.; Malmqvist, P. A.; Neogrády, P.; Pedersen, T. B.; Pitonák, M.; Reiher, M.; Roos, B. O.; Serrano-Andrés, L.; Urban, M.; Veryazov, V.; Lindh, R. *J. Comput. Chem.* **2010**, *31*, 224–47.
- (57) Werner, H. J.; Knowles, P. J.; Knizia, G.; Manby, F. R.; Schütz, M.; Celani, P.; Korona, T.; Lindh, R.; Mitrushenkov, A.; Rauhut, G.; Shamasundar, K. R.; Adler, T. B.; Amos, R. D.; Bernhardsson, A.; Berning, A.; Cooper, D. L.; Deegan, M. J. O.; Dobbyn, A. J.; Eckert, F.; Goll, E.; Hampel, C.; Hesselmann, A.; Hetzer, G.; Hrenar, T.; Jansen, G.; Köppl, C.; Liu, Y.; Lloyd, A. W.; Mata, R. A.; May, A. J.; McNicholas, S. J.; Meyer, W.; Mura, M. E.; Nicklass, A.; O'Neill, D. P.; Palmieri, P.; Pflüger, K.; Pitzer, R.; Reiher, M.; Shiozaki, T.; Stoll, H.; Stone, A. J.; Tarroni, R.; Thorsteinsson, T.; Wang, M.; Wolf, A. *MOLPRO*, version 2010.1; Cardiff University: Cardiff, U. K.; Universität Stuttgart: Stuttgart, Germany, 2010.
- (58) Langhoff, S. R.; Davidson, E. R. *Int. J. Quantum Chem.* **1974**, *8*, 61–72.
- (59) Werner, H. J.; Kállay, M.; Gauss, J. *J. Chem. Phys.* **2008**, *128*, 034305.
- (60) Shao, Y.; Molnar, L. F.; Jung, Y.; Kussmann, J.; Ochsenfeld, C.; Brown, S. T.; Gilbert, A. T.; Slipchenko, L. V.; Levchenko, S. V.; O'Neill, D. P.; DiStasio, R. A.; Lochan, R. C.; Wang, T.; Beran, G. J.; Besley, N. A.; Herbert, J. M.; Lin, C. Y.; Van Voorhis, T.; Chien, S. H.; Sodt, A.; Steele, R. P.; Rassolov, V. A.; Maslen, P. E.; Korambath, P. P.; Adamson, R. D.; Austin, B.; Baker, J.; Byrd, E. F.; Dachsels, H.; Doerksen, R. J.; Dreuw, A.; Dunietz, B. D.; Dutoi, A. D.; Furlani, T. R.; Gwaltney, S. R.; Heyden, A.; Hirata, S.; Hsu, C. P.; Kedziora, G.; Khalliulin, R. Z.; Klunzinger, P.; Lee, A. M.; Lee, M. S.; Liang, W.; Lotan, I.; Nair, N.; Peters, B.; Proynov, E. I.; Pieniazek, P. A.; Rhee, Y. M.; Ritchie, J.; Rosta, E.; Sherrill, C. D.; Simmonett, A. C.; Subotnik, J. E.; Woodcock, H. L.; Zhang, W.; Bell, A. T.; Chakraborty, A. K.; Chipman, D. M.; Keil, F. J.; Warshel, A.; Hehre, W. J.; Schaefer, H. F.; Kong, J.; Krylov, A. I.; Gill, P. M.; Head-Gordon, M. *Phys. Chem. Chem. Phys.* **2006**, *8*, 3172–91.
- (61) Atchity, G. J.; Xantheas, S. S.; Ruedenberg, K. *J. Chem. Phys.* **1991**, *95*, 1862.